ELSEVIER

Journal of Fluids and Structures 20 (2005) 1085–1104

JOURNAL OF FLUIDS AND STRUCTURES

www.elsevier.com/locate/jfs

Vortex-induced oscillations at low Reynolds numbers: Hysteresis and vortex-shedding modes

S.P. Singh, S. Mittal*

Department of Aerospace Engineering, Indian Institute of Technology Kanpur, Kanpur, UP 208 016, India

Received 15 April 2004; accepted 20 May 2005

Abstract

Results are presented for the numerical simulation of vortex-induced vibrations (VIVs) of a cylinder at low Reynolds numbers (Re). A stabilized space–time finite-element formulation is utilized to solve the incompressible flow equations in primitive variables. The cylinder, of low nondimensional mass ($m^* = 10$), is free to vibrate in, both, the transverse and in-line directions. To investigate the effect of Re and reduced natural frequency, F_n, two sets of computations are carried out. In the first set of computations the Reynolds number is fixed ($= 100$) and the reduced velocity ($U^* = 1/F_n$) is varied. Hysteresis, in the response of the cylinder, is observed at the low- as well as high-end of the range of reduced velocity for *synchronization/lock-in*. In the second set of computations, the effect of Reynolds number ($50 \leqslant \mathrm{Re} \leqslant 500$) is investigated for a fixed reduced velocity ($U^* = 4.92$). The effect of the Reynolds number is found to be very significant for VIVs. While the vortex-shedding mode at low Re is 2S (two single vortices shed per cycle), at Re$\sim$300 and larger, the P + S mode of vortex shedding (a single vortex and one pair of counter-rotating vortices are released in each cycle of shedding) is observed. This is the first time that the P + S mode has been observed for a cylinder undergoing free vibrations. This change of vortex-shedding mode is hysteretic in nature and results in a very large increase in the amplitude of in-line oscillations. Since the flow ceases to remain two-dimensional beyond Re$\sim$200, it remains to be seen whether the P + S mode of shedding can actually be observed in reality for free vibrations.

Keywords: Unsteady flows; Hysteresis; Vortex shedding; Finite elements

1. Introduction

The flow past a stationary circular cylinder becomes unstable beyond Re$\sim$47 (Williamson, 1996) and vortex-shedding ensues. As a result, the cylinder experiences unsteady aerodynamic forces that may lead to vortex-induced vibrations (VIV). It is well known that the motion of the cylinder can alter the flow-field significantly. Under certain conditions, the motion can cause the vortex-shedding frequency to match the vibration frequency. This is referred to as *lock-in* or *synchronization*. In addition, near the low- and high-end of the *lock-in* regime, the flow and cylinder response may exhibit *hysteresis*. Significant research has contributed to the understanding of various phenomena associated with VIV. For a comprehensive review of the research, on various aspects of VIV, the reader is referred to a recent article by Williamson and Govardhan (2004).

*Corresponding author.
E-mail address: smittal@iitk.ac.in (S. Mittal).

0889-9746/$ - see front matter
doi:10.1016/j.jfluidstructs.2005.05.011

Khalak and Williamson (1999) carried out VIV experiments using a setup with low mass–damping ($m^*\zeta$, where m^* is the nondimensional mass and ζ is the damping ratio). They found that, depending on the value of $m^*\zeta$, the response of the system is one of the two types. For low mass–damping, the response consists of three branches: an initial excitation branch, and upper and lower branches. The mode transition between the initial and upper branches is hysteretic, while that between the upper and lower branches is associated with intermittent switching of phase. With the help of flow visualization they found that the initial branch is associated with the 2S mode of shedding (Williamson and Roshko, 1988) while the lower branch corresponds with the 2P mode. In the 2S mode of shedding (the classic Karman street), two single vortices per cycle are released from the cylinder. In the 2P mode, two vortex pairs are formed and released during each cycle of vortex shedding. Hysteresis with respect to the transition between the initial excitation and upper branches is observed for a range of reduced velocity ($U^* = 4.45-4.70$). The reduced velocity, U^* is defined as U_∞/fD, where U_∞ is the free-stream speed, D is the diameter of the cylinder and f is the vibrating frequency of the body. For high values of $m^*\zeta$, only two response branches exist.

Brika and Laneville (1993) conducted VIV experiments for a long flexible cylinder with low mass–damping. They observed that the transverse displacement of the cylinder is hysteretic with the variation of flow-velocity. The velocity of the flow was varied in two ways: progressive and impulsive. Two branches of cylinder response exist. The upper and lower branches of the cylinder response are associated with different modes of vortex shedding. The upper branch is realized when the velocity is increased in a progressive way with small increments. In this case the 2S mode of vortex shedding is observed. The lower branch is obtained when the velocity is either decreased in progressive manner or changed impulsively. This branch is associated with the 2P vortex-shedding mode as suggested by Williamson and Roshko (1988) via their experiments for forced oscillation of a cylinder.

Mittal and Tezduyar (1992) carried out VIV studies for a cylinder, restricted to transverse oscillation, using a finite element method for $290 \leqslant \mathrm{Re} \leqslant 360$. They observed the phenomena of *hysteresis* and *lock-in* in their simulations. For a certain range of Reynolds number, a low- or high-vibration amplitude solution can be realized depending upon the initial condition. They showed, using data for forced oscillations from Koopmann (1967), that the *hysteresis*, observed in their computations, is a consequence of lock-in. In the context of forced oscillations, it is known that lock-in occurs only if the vibration amplitude of the cylinder is greater than a certain threshold value (Koopmann, 1967). For a certain range of Reynolds number, if the initial condition corresponds to a cylinder vibrating with large amplitude that is beyond the threshold value for lock-in, the vortex-shedding frequency locks-in to the structural frequency and one realizes a high-amplitude solution. On the other hand, if one begins with a solution that corresponds to low-amplitude oscillations, that is below the threshold required for lock-in, a low-amplitude solution is realized.

Mittal and Kumar (1999) studied VIV of a cylinder with, both, in-line and transverse oscillations at $\mathrm{Re} = 325$. Computations were carried out for various values of the reduced natural frequency ($F_n = f_n D/U_\infty$, where f_n is the natural frequency of the system). Lock-in is observed for a range of values of F_n. Over a certain range of structural frequency, the vortex-shedding frequency of the oscillating cylinder does not match F_n exactly; there is a slight *detuning*. This phenomenon is referred to as *soft-lock-in*. It was shown that this detuning disappears when the mass of the cylinder is significantly larger than the mass of the surrounding fluid it displaces. It has also been pointed out by Khalak and Williamson (1999) that, for low m^*, synchronization is defined by the matching of the vortex-shedding and cylinder vibration frequencies. In general, at synchronization, the vortex-shedding frequency can be quite different than the natural frequency.

Blackburn and Henderson (1996) presented numerical results for forced and free vibrations of a cylinder at $\mathrm{Re} = 250$. For free vibrations, lock-in is observed for a range of natural frequencies. A chaotic cylinder response is also seen for certain frequencies. With forced vibrations of the cylinder, they observed the P + S mode of shedding for $\mathrm{Re} = 140$ with oscillation amplitude of $0.75D$ and higher.

Guilmineau and Queutey (2001) simulated the VIV of an elastically mounted rigid cylinder with low mass–damping. The cylinder was restricted to oscillate only in the direction transverse to the flow. The Reynolds number was varied from 900 to 15 000 and the corresponding reduced velocity, U^*, between 1.0 and 17.0. To account for the turbulence at large Re, Large Eddy Simulation was employed using the SST K–ω model of Menter. The nondimensional mass and damping for the system correspond to $m^* = 2.4$ and $m^*\zeta = 0.013$. Computations were carried out using three sets of initial conditions: (a) *from rest*, (b) *increasing velocity* and (c) *decreasing velocity*. Small increments of the reduced velocity (U^*) were used to conduct the studies with increasing and decreasing velocity. The response of the vibrating cylinder was found to depend on the initial conditions. Only the lower branch was predicted with the *from rest* and decreasing velocity initial conditions. With the *increasing velocity* initial condition, the maximum amplitude corresponds to the value obtained experimentally, but the upper branch does not match experimental results.

Jauvtis and Williamson (2003) studied the behavior of an elastically mounted cylinder with, both, streamwise and transverse motions. The range of values of m^* in their study is 5–25. The system has the same natural frequency ($f_N = 0.4$ Hz) in both the directions. It was found that the freedom of the body to oscillate in both the directions has

very little effect on the transverse response of the system and the vortex wake dynamics. Compared to the transverse-only motion, the peak of the upper branch of the transverse motion for the case where both motions are allowed increases by 10%.

Williamson and Govardhan (2004) compiled data from various researchers for VIV in the laminar vortex-shedding range and demonstrated that the hysteresis at the low-velocity end of the synchronization regime may exist. The maximum amplitude for transverse oscillations at low Re, in the laminar vortex-shedding range, is significantly smaller than that observed at large Re. Anagnostopoulos and Bearman (1992) conducted free-vibration experiments for $\mathrm{Re} = 90-150$. There is good agreement between the amplitudes from their experiments and those from the two-dimensional simulations by various researchers for $\mathrm{Re} = 100-200$.

In this paper, we present our results for VIV of a cylinder at low Reynolds numbers. The oscillator system has very low nondimensional mass ($m^* = 10$) and the structural damping coefficient is assigned a zero value. The cylinder is allowed to vibrate in, both, transverse and in-line directions. Typical experiments in a laboratory setup are conducted for an oscillator, of given mass and spring-stiffness, by varying the flow speed. In such a scenario, it can be seen that, the reduced natural frequency, $F_n = 1/U^*$, varies inversely with Re. To investigate the effect of Re and F_n on the oscillator, independently, two sets of computations are carried out. In the first set of computations the Reynolds number is fixed ($= 100$) and the reduced velocity (U^*) is varied. For a range of values of U^*, lock-in takes place. Hysteresis is observed at the low- as well as high-velocity end of the synchronization regime. Maximum amplitude of transverse oscillations is seen for $U^* \sim 4.75$. In the second set of computations, the reduced velocity of the system is fixed at $U^* = 4.92$ and the effect of Reynolds number ($50 \leqslant \mathrm{Re} \leqslant 500$) is investigated. Hysteresis, with respect to increasing and decreasing the Reynolds number, is seen again at the low-Re end of the lock-in regime. In addition, a hysteretic jump in the mode of vortex shedding is observed at $\mathrm{Re} \sim 300$.

2. The governing equations

2.1. The incompressible flow equations

Let $\Omega_t \subset \mathbb{R}^{n_{sd}}$ and $(0, T)$ be the spatial and temporal domains, respectively, where n_{sd} is the number of space dimensions, and let Γ_t denote the boundary of Ω_t. The spatial and temporal coordinates are denoted by $\mathbf{x}$ and t. The Navier–Stokes equations governing incompressible fluid flow are

$$\rho\left(\frac{\partial \mathbf{u}}{\partial t} + \mathbf{u}\cdot\boldsymbol{\nabla}\mathbf{u} - \mathbf{f}\right) - \boldsymbol{\nabla}\cdot\boldsymbol{\sigma} = 0 \quad \text{on } \Omega_t \quad \text{for } (0, T), \tag{1}$$

$$\boldsymbol{\nabla}\cdot\mathbf{u} = 0 \quad \text{on } \Omega_t \quad \text{for } (0, T). \tag{2}$$

Here ρ, $\mathbf{u}$, $\mathbf{f}$ and $\boldsymbol{\sigma}$ are the density, velocity, body force and the stress tensor, respectively. The stress tensor is written as the sum of its isotropic and deviatoric parts

$$\boldsymbol{\sigma} = -p\mathbf{I} + \mathbf{T}, \quad \mathbf{T} = 2\mu\boldsymbol{\varepsilon}(\mathbf{u}), \quad \boldsymbol{\varepsilon}(\mathbf{u}) = \tfrac{1}{2}((\boldsymbol{\nabla}\mathbf{u}) + (\boldsymbol{\nabla}\mathbf{u})^{\mathrm{T}}), \tag{3}$$

where p and μ are the pressure and dynamic viscosity, respectively. Both the Dirichlet and Neumann-type boundary conditions are accounted for, represented as

$$\mathbf{u} = \mathbf{g} \text{ on } (\Gamma_t)_g, \quad \mathsf{n}\cdot\boldsymbol{\sigma} = \mathbf{h} \quad \text{on } (\Gamma_t)_h, \tag{4}$$

where $(\Gamma_t)_g$ and $(\Gamma_t)_h$ are complementary subsets of the boundary Γ_t and n is its unit normal vector. The initial condition on the velocity is specified on Ω_t at $t = 0$:

$$\mathbf{u}(\mathbf{x}, 0) = \mathbf{u}_0 \quad \text{on } \Omega_0, \tag{5}$$

where $\mathbf{u}_0$ is divergence free.

2.2. The equations of motion for a rigid body

A solid body immersed in the fluid experiences unsteady forces and in certain cases may exhibit rigid body motion. The motion of the body, in the two directions along the Cartesian axes, is governed by the following equations:

$$\ddot{X} + 4\pi F_n\zeta\dot{X} + (2\pi F_n)^2 X = \frac{2C_D}{\pi m^*} \quad \text{for } (0, T), \tag{6}$$

$$\ddot{Y} + 4\pi F_n \zeta \dot{Y} + (2\pi F_n)^2 Y = \frac{2C_L}{\pi m^*} \quad \text{for } (0, T). \tag{7}$$

Here, F_n is the reduced natural frequency of the oscillator, ζ the structural damping ratio, m^* the nondimensional mass of the body while C_L and C_D are the instantaneous lift and drag coefficients for the body, respectively. The free-stream flow is assumed to be along the x-axis. $\ddot{X}$, $\dot{X}$ and X denote the normalized in-line acceleration, velocity and displacement of the body, respectively, while $\ddot{Y}$, $\dot{Y}$ and Y represent the same quantities associated with the cross-flow motion. In the present study, in which the rigid body is a circular cylinder, the displacement and velocity are normalized by the diameter, D, of the cylinder and the free-stream speed, U_∞, respectively. The reduced natural frequency of the system, F_n is defined as $f_n D/U_\infty$, where f_n is the natural frequency of the oscillator. Another related parameter is the reduced velocity, U^*. It is defined as $U^* = U_\infty/f_n D = 1/F_n$.

The nondimensional mass of the cylinder is defined as $m^* = 4m/\pi\rho_\infty D^2$, where m is the actual mass of the oscillator per unit length and ρ_∞ is the density of the fluid. The force coefficients are computed by carrying an integration, that involves the pressure and viscous stresses, around the circumference of the cylinder:

$$C_D = \frac{1}{\frac{1}{2}\rho_\infty U_\infty^2 D} \int_{\Gamma_{\text{cyl}}} (\boldsymbol{\sigma}\mathsf{n}) \cdot \mathsf{n}_\mathsf{x} \, \mathrm{d}\Gamma \tag{8}$$

$$C_L = \frac{1}{\frac{1}{2}\rho_\infty U_\infty^2 D} \int_{\Gamma_{\text{cyl}}} (\boldsymbol{\sigma}\mathsf{n}) \cdot \mathsf{n}_\mathsf{y} \, \mathrm{d}\Gamma. \tag{9}$$

Here n_x and n_y are the cartesian components of the unit vector n that is normal to the cylinder boundary Γ_{cyl}.

3. The finite-element formulation

To accommodate the motion of the cylinder and the deformation of the mesh, a formulation that can handle moving boundaries and interfaces is employed. In order to construct the finite-element function spaces for the space–time method, we partition the time interval $(0, T)$ into subintervals $I_n = (t_n, t_{n+1})$, where t_n and t_{n+1} belong to an ordered series of time levels: $0 = t_0 < t_1 < \cdots < t_N = T$. Let $\Omega_n = \Omega_{t_n}$ and $\Gamma_n = \Gamma_{t_n}$. We define the space–time slab Q_n as the domain enclosed by the surfaces Ω_n, Ω_{n+1}, and P_n, where P_n is the surface described by the boundary Γ_t as t traverses I_n. As is the case with Γ_t, the surface P_n is decomposed into $(P_n)_g$ and $(P_n)_h$ with respect to the type of boundary condition (Dirichlet or Neumann) being imposed. For each space–time slab we define the corresponding finite-element function spaces: $(\mathscr{S}^h_{\mathbf{u}})_n$, $(\mathscr{V}^h_{\mathbf{u}})_n$, $(\mathscr{S}^h_p)_n$, and $(\mathscr{V}^h_p)_n$. Over the element domain, this space is formed by using first-order polynomials in space and time. Globally, the interpolation functions are continuous in space but discontinuous in time.

The stabilized space–time formulation for deforming domains is then written as follows: given $(\mathbf{u}^h)_{n^-}$, find $\mathbf{u}^h \in (\mathscr{S}^h_{\mathbf{u}})_n$ and $p^h \in (\mathscr{S}^h_p)_n$, such that $\forall \mathbf{w}^h \in (\mathscr{V}^h_{\mathbf{u}})_n$, $q^h \in (\mathscr{V}^h_p)_n$,

$$\begin{aligned}
&\int_{Q_n} \mathbf{w}^h \cdot \rho\left(\frac{\partial \mathbf{u}^h}{\partial t} + \mathbf{u}^h \cdot \boldsymbol{\nabla}\mathbf{u}^h - \mathbf{f}\right) \mathrm{d}\Omega + \int_{Q_n} \boldsymbol{\varepsilon}(\mathbf{w}^h) : \boldsymbol{\sigma}(p^h, \mathbf{u}^h) \, \mathrm{d}Q + \int_{Q_n} q^h \boldsymbol{\nabla} \cdot \mathbf{u}^h \, \mathrm{d}Q \\
&\quad + \sum_{e=1}^{n_{el}} \int_{Q_n^e} \frac{1}{\rho} \tau \left[\rho\left(\frac{\partial \mathbf{w}^h}{\partial t} + \mathbf{u}^h \cdot \boldsymbol{\nabla}\mathbf{w}^h\right) - \boldsymbol{\nabla} \cdot \boldsymbol{\sigma}(q^h, \mathbf{w}^h)\right] \\
&\quad \cdot \left[\rho\left(\frac{\partial \mathbf{u}^h}{\partial t} + \mathbf{u}^h \cdot \boldsymbol{\nabla}\mathbf{u}^h - \mathbf{f}\right) - \boldsymbol{\nabla} \cdot \boldsymbol{\sigma}(p^h, \mathbf{u}^h)\right] \mathrm{d}Q \\
&\quad + \sum_{e=1}^{n_{el}} \int_{Q_n^e} \delta \boldsymbol{\nabla} \cdot \mathbf{w}^h \rho \boldsymbol{\nabla} \cdot \mathbf{u}^h \, \mathrm{d}Q + \int_{\Omega_n} (\mathbf{w}^h)_n^+ . \rho((\mathbf{u}^h)_n^+ - (\mathbf{u}^h)_n^-) \, \mathrm{d}\Omega \\
&\quad = \int_{(P_n)_h} \mathbf{w}^h \cdot \mathbf{h}^h \, \mathrm{d}P.
\end{aligned} \tag{10}$$

This process is applied sequentially to all the space–time slabs $Q_0, Q_1, \ldots, Q_{N-1}$. In the variational formulation given by Eq. (10), the following notation is being used:

$$(\mathbf{u}^h)_n^{\pm} = \lim_{\varepsilon \to 0} \mathbf{u}(t_n \pm \varepsilon), \tag{11}$$

$$\int_{Q_n} (\ldots)\,\mathrm{d}Q = \int_{I_n}\int_{\Omega_n} (\ldots)\,\mathrm{d}\Omega\,\mathrm{d}t, \tag{12}$$

$$\int_{P_n} (\ldots)\,\mathrm{d}P = \int_{I_n}\int_{\Gamma_n} (\ldots)\,\mathrm{d}\Gamma\,\mathrm{d}t. \tag{13}$$

The computations start with

$$(\mathbf{u}^h)_0^- = \mathbf{u}_0, \tag{14}$$

where $\mathbf{u}_0$ is divergence free.

The variational formulation given by Eq. (10), includes certain stabilization terms added to the basic Galerkin formulation to enhance its numerical stability. Details on the formulation, including the definitions of the coefficients τ and δ, can be found in the papers by Tezduyar et al. (1992a–c).

The equations of motion for the oscillator given by Eq. (6)–(7) are also cast in the space–time formulation in the same manner as described in the work by Tezduyar et al. (1992b) and Mittal (1992).

4. Problem description

The cylinder, mounted on elastic supports, is allowed to vibrate, both, in the streamwise and transverse directions. The nondimensional mass of the cylinder is $m^* = 10.0$. To encourage high-amplitude oscillations, the structural damping coefficient is set to zero. The Reynolds number, Re, is based on the free-stream speed, diameter of the cylinder and viscosity of the fluid. The springs in, both, the transverse and in-line directions are assumed to be linear and with same stiffness.

It is interesting to note that the reduced natural frequency, F_n ($= 1/U^*$), that appears in Eqs. (6) and (7), for a given spring–mass system varies inversely with Re. In that sense, for a certain spring–mass system, F_n and Re are not independent parameters. However, it would be useful to study their effect on VIV by varying them independently. This can certainly be done in the framework of numerical simulations. To this extent, in the present work, two sets of computations are carried out. In the first set of computations, the Reynolds number is set to 100 and the reduced velocity, U^*, is varied. The maximum amplitude for transverse oscillations are observed for $U^* \sim 4.75$. The second set of computations are carried out with the objective of investigating the effect of Reynolds number when the cylinder vibrates at, approximately, its maximum amplitude. Therefore, in the second set of computations, the reduced velocity of the system is fixed at $U^* = 4.92$ while the Reynolds number is varied.

4.1. Boundary conditions

No slip condition is applied for the velocity at the cylinder boundary. The flow velocity on the cylinder surface and the location of the cylinder are updated at each nonlinear interaction by solving the of motion for the oscillator. Free-stream values are assigned for the velocity at the upstream boundary and the viscous stress vector is equal to zero at the downstream boundary. On the upper and lower boundaries, the component of velocity normal to and the component of stress vector along these boundaries are prescribed zero value.

4.2. Finite-element mesh and the mesh moving scheme

The finite-element mesh, utilized for many of the computations in this paper, is shown in Fig. 1. It consists of 7437 nodes and 7236 quadrilateral, four-noded elements. We refer to this mesh as Mesh $M7k$. The cylinder resides in a rectangular computational domain whose upstream and downstream boundaries are located at 10 and 25.5 cylinder diameters from the center of the cylinder, respectively. The upper and lower boundaries are placed at 10 diameters from the center of the cylinder.

The mesh moving scheme has been designed such that the mesh in the square box around the cylinder moves along with it as a rigid body. The location of the outer boundary is fixed. As a result, the movement of the cylinder causes deformation of the mesh points lying between the square region and the outer boundary. This kind of a mesh movement is expected to lead to almost no projection errors in the flow close to the cylinder. The issue of adequacy of the spatial resolution of this mesh is addressed via comparison of results for different resolutions, later in the article. It was also

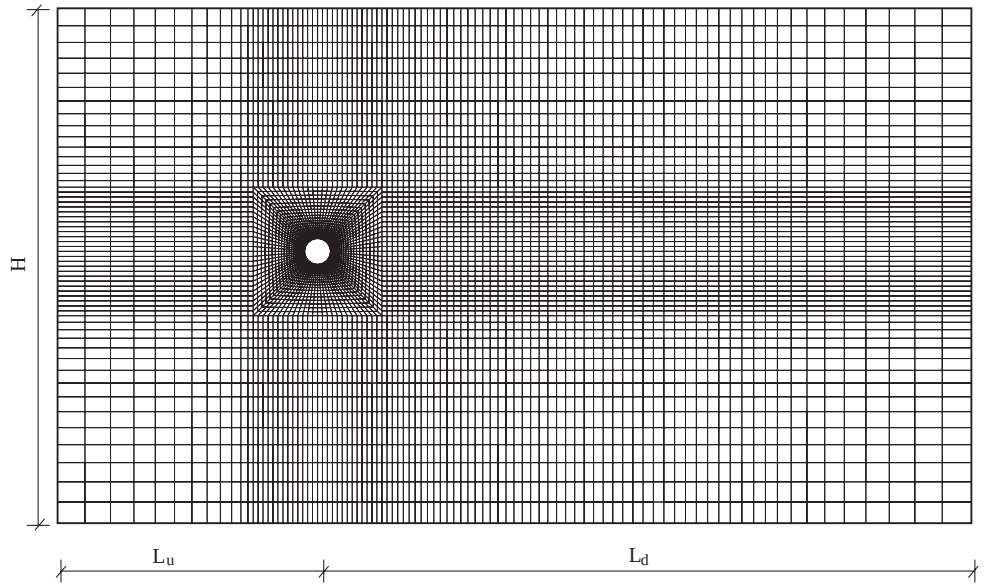

Fig. 1. The finite-element mesh: 7437 nodes and 7236 quadrilateral elements.

studied in one of our earlier papers (Mittal and Kumar, 1999). A time step size of 0.0625 is employed for the present computations.

5. Results

Equal-in-order basis functions for velocity and pressure, that are bilinear in space and linear in time, are used and $2 \times 2 \times 2$ Gaussian quadrature is employed for numerical integration. The nonlinear equation systems resulting from the finite-element discretization of the flow equations are solved using the Generalized Minimal RESidual (*GMRES*) technique in conjunction with diagonal preconditioners.

In all the figures for the vorticity field, presented in this article, a gray scale, based on the magnitude of the vorticity, is used for *shading*. The darker shades of gray represents higher value of vorticity. To differentiate between the positive and negative values, iso-vorticity contours are also shown. Black colored contour lines represent negative, while the white colored lines show positive values of the vorticity field.

5.1. Re = 100, *flow past a stationary cylinder*

Computations for a stationary cylinder at Re = 100 are carried out till the flow reaches a temporally periodic solution. The value of Strouhal number (St), mean drag coefficient, $\overline{C_D}$ and r.m.s. value of the lift coefficient, $C_{L_{\text{r.m.s.}}}$ obtained are 0.163, 1.31 and 0.25, respectively. The values obtained for a more refined mesh (Mesh $M18k$) with 18 220 nodes and 17 904 elements, are 0.166, 1.35 and 0.25, respectively. The experimental value of St reported by Williamson (1989) is 0.1648 for parallel shedding, while Kravchenko et al. (1999) and Persillon and Braza (1998) have reported St = 0.164 from their simulations. $\overline{C_D}$ from present computation compares quite well with the value reported by Henderson (1995) (= 1.35). This shows that the mesh with 7437 nodes gives reasonably accurate solutions, at least for flow past a stationary cylinder. A similar study for a vibrating cylinder is presented in a later section.

5.2. *Vortex-induced vibrations:* Re = 100, *variation with* U^*

5.2.1. *Overview of the cylinder response*

Figs. 2–5 show the variation of displacement of the cylinder and aerodynamic coefficients with U^*. The amplitude of transverse vibrations is significantly higher than those of the in-line oscillations. The peak amplitude of vibration is,

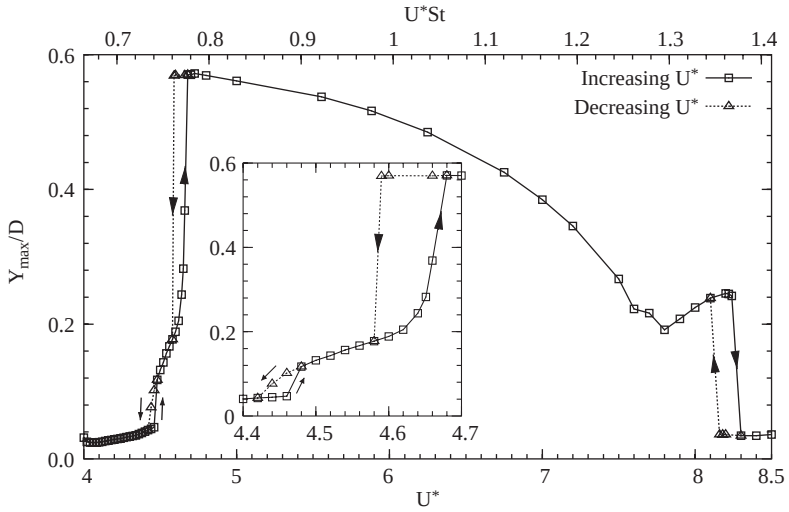

Fig. 2. Vortex-induced vibrations at $Re = 100$: variation of the maximum transverse displacement of the cylinder with reduced velocity, U^* & U^*St. Here, St is the Strouhal number for the stationary cylinder at $Re = 100$.

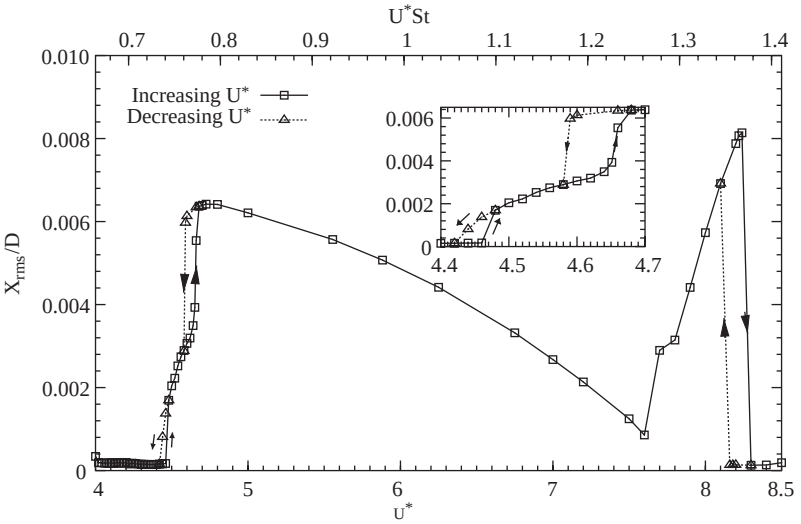

Fig. 3. Vortex-induced vibrations at $Re = 100$: variation of the r.m.s. value of in-line displacement of the cylinder with reduced velocity, U^* & U^*St. Here, St is the Strouhal number for the stationary cylinder at $Re = 100$.

$0.6D$, approximately and is achieved for $U^*St \sim 0.78$ (where, St is the Strouhal number for the stationary cylinder at $Re = 100$). The response of the cylinder transverse to the flow direction is very similar to that reported by other researchers, for low Re flow, as summarized by Williamson and Govardhan (2004). However, there are a few differences. The present computations result in a hysteretic behavior at, both, the lower and higher range of flow synchronization. Here, we wish to point out that to avoid clutter in the figures, only that data, corresponding to decreasing U^*, has been shown that is necessary to point out the hysteresis in the cylinder response and flow. The close-up views in the insets of Figs. 2 and 3 show the details of the hysteresis in the lower range of U^*. Two hysteretic loops can be clearly seen in these figures. It has been pointed out by Brika and Laneville (1993) that the cylinder response is quite sensitive to the increments in reduced velocity, ΔU^*. Keeping that in mind, computations for $4 < U^* < 4.7$ have been carried out with increments of $\Delta U^* = 0.02$.

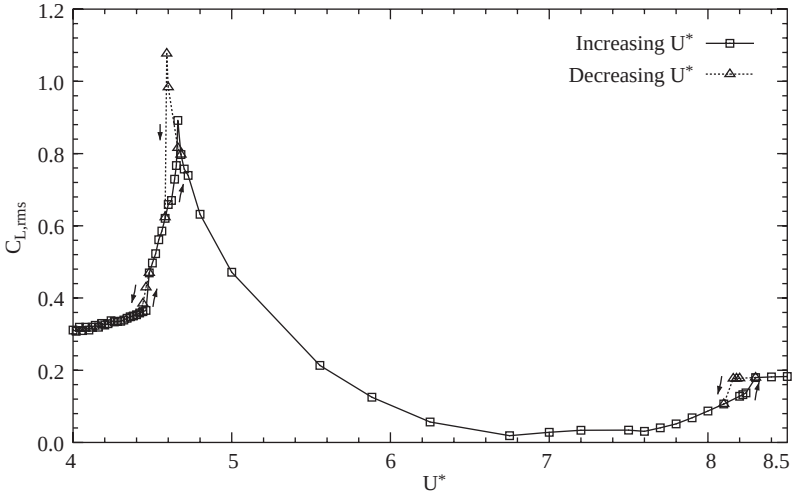

Fig. 4. Vortex-induced vibrations at Re = 100: variation of the r.m.s. value of lift coefficient with reduced velocity, U^*.

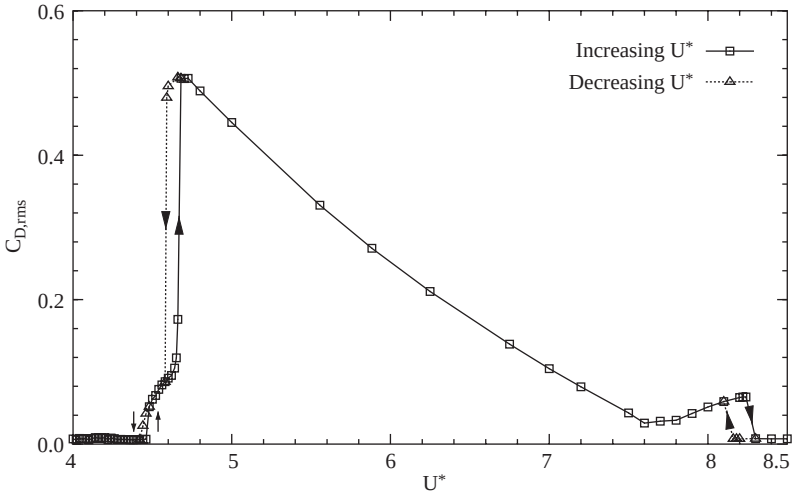

Fig. 5. Vortex-induced vibrations at Re = 100: variation of the r.m.s. value of drag coefficient with reduced velocity, U^*.

The r.m.s. values of the lift and drag coefficients for the vibrating cylinders also show hysteretic jumps. As a result of vibrations, compared to a stationary cylinder, the r.m.s. value of the force coefficients is quite high for certain values of U^*. In addition, modulation (beating) is observed in the time histories of the force coefficients. The response of the cylinder appears to be associated with another peak at $U^* \sim 8.3$. The amplitude of the in-line oscillations for the second peak are slightly larger than that for the first peak at $U^* \sim 4.6$. It is interesting to note that although the amplitude of in-line oscillations is larger for the second peak, the unsteady component of the drag coefficient is significantly larger for the first peak. In general, the vibration of the cylinder results in a large increase in unsteady component of the drag coefficient.

Fig. 6 shows the variation of the reduced frequency of transverse oscillations of the cylinder with U^*. Also shown in the same figure is the reduced natural frequency, $F_n = 1/U^*$. The broad range of synchronization/lock-in for $4.6 < U^* < 8.2$, approximately, is quite apparent from this figure. Our computations indicate that the vortex-shedding frequency is quite close to the cylinder vibration frequency. In this range of reduced velocity, the vibrations of the cylinder cause the vortex-shedding frequency to assume the same value as the natural frequency of the spring–mass

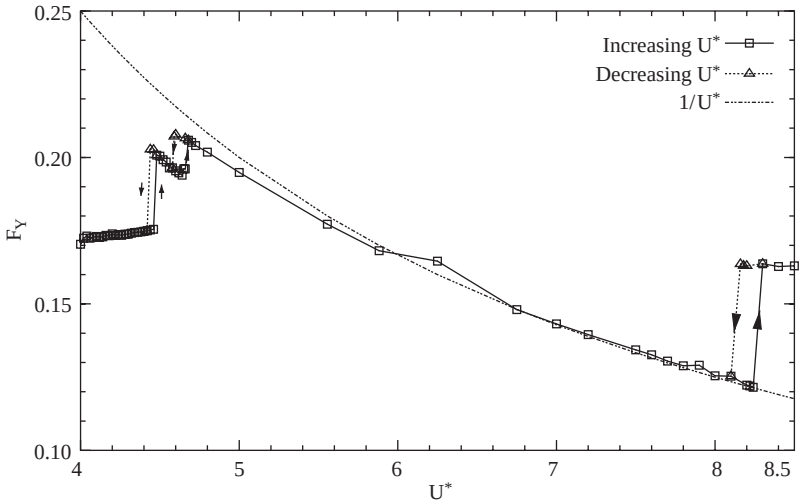

Fig. 6. Vortex-induced vibrations at Re = 100: variation of the reduced frequency of transverse oscillations of the cylinder with reduced velocity, U^*. Also shown is the reduced natural frequency, $F_n = 1/U^*$.

system. Two hysteretic loops at the lower end of synchronization velocity ($4.42 \geqslant U^* \geqslant 4.48$ and $4.58 \geqslant U^* \geqslant 4.68$) and one at the higher end ($8.1 \geqslant U^* \geqslant 8.3$) are clearly observed in Fig. 6. Beyond the range of U^* for lock-in, the vortex-shedding frequency moves back to that for a stationary cylinder (~0.163).

5.2.2. Hysteresis and modes of vortex shedding

Fig. 7 shows the instantaneous vorticity fields for various U^*. In all the cases the 2S mode of vortex shedding, as described by Williamson and Roshko (1988), is observed. In this mode of shedding, during each vortex-shedding cycle, a single vortex is alternately shed from each side of the cylinder. For those values of U^*, where the cylinder executes high-amplitude transverse vibrations (for example, $U^* = 5$), the vortices in the wake coalesce giving rise to the C(2S) mode of vortex shedding. The two solutions at $U^* = 4.6$, for increasing and decreasing reduced velocity, are also shown in Fig. 7. As expected, the flow for the case with high-amplitude oscillations is very similar to that for $U^* = 5.0$ while the one with lower amplitude vibrations, or increasing U^*, resembles the flow for a stationary cylinder. The time histories of the aerodynamic coefficients and the cylinder response are shown in Figs. 8 and 9.

For increasing U^* (or decreasing F_n), in the range of synchronization, the reduction in the vortex-shedding frequency can be observed from Fig. 7 from the increased longitudinal spacing between the vortices. $U^* = 8.22$ lies at the far end of the synchronization regime. At this value of reduced velocity the vortex-shedding frequency for the vibrating cylinder switches between the natural frequency of the oscillator and the vortex-shedding frequency for the stationary cylinder.

5.2.3. Are the in-line oscillations responsible for the hysteretic behavior at high U^*?

The peak at $U^* \sim 8.3$ in the response of the cylinder in in-line and transverse directions and their hysteretic behavior has not been observed by earlier investigators. However, most efforts have been for a cylinder restricted to transverse oscillations. Therefore, one is tempted to attribute this behavior to in-line oscillations. To address this issue, two sets of computations were carried out. The fully developed unsteady solutions for $U^* = 8.20$ corresponding to increasing and decreasing reduced velocity are utilized as initial conditions to compute flow past a cylinder restricted to vibrate (a) in in-line direction only and (b) in transverse direction only. It is observed that when the cylinder is restricted to in-line vibrations, both the initial conditions lead to a low-amplitude solution. The fully developed unsteady flow is very similar to that for a stationary cylinder. On the other hand, in the case where the cylinder is allowed to vibrate in the transverse direction only, the hysteretic behavior persists. The solutions obtained in this case are very similar to those seen for a cylinder that is free to vibrate in both in-line and transverse oscillations. This suggests that it is not the in-line oscillations that cause the hysteretic behavior of the

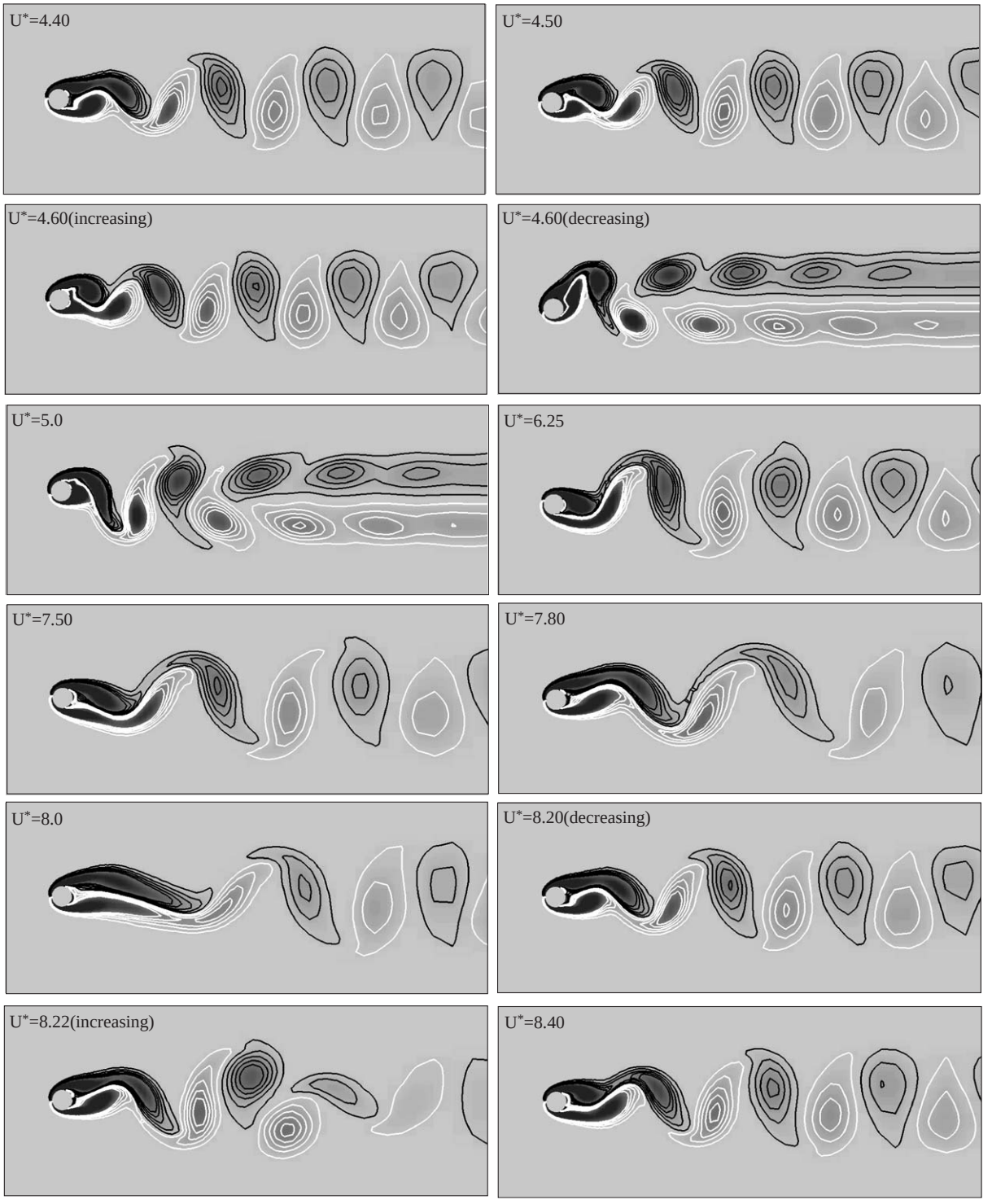

Fig. 7. Vortex-induced vibrations at Re = 100: instantaneous vorticity field at various values of reduced velocity, U^*.

flow at the end of synchronization range of U^*. This is consistent with the observation made by Jauvtis and Williamson (2003) that, for $m^* > 5$, the freedom to oscillate in-line with the flow has very little effect on the transverse vibrations.

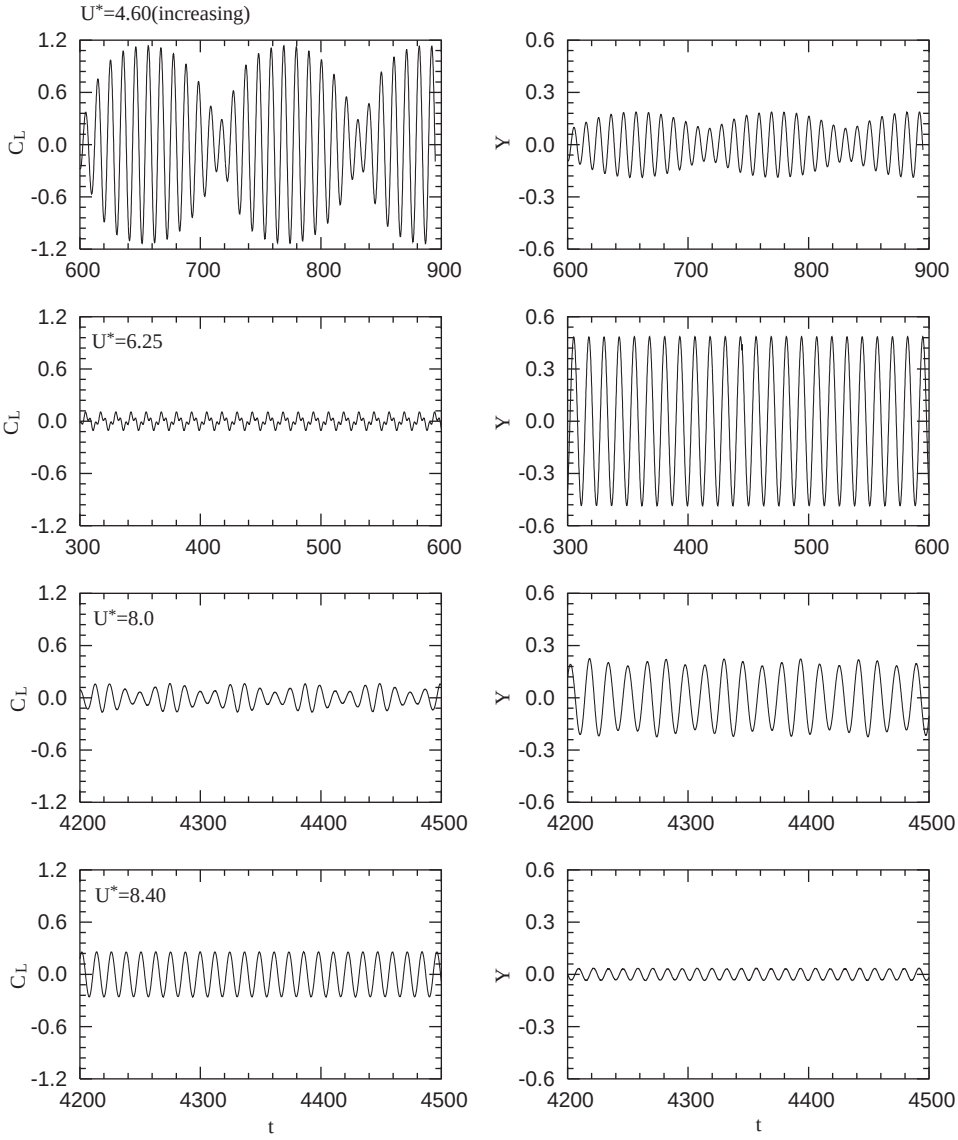

Fig. 8. Vortex-induced vibrations at Re = 100: time histories of the lift coefficient and normalized transverse displacement of the cylinder for various values of reduced velocity, U^*.

5.3. *Vortex induced vibrations:* $U^* = 4.92$*, variation with* Re

To investigate the effect of Re on VIV, computations are carried out for various values of Re while the reduced velocity is fixed at $U^* = 4.92$. At this value of $U^* = 4.92$, the cylinder vibrates at close to maximum amplitude observed for Re = 100. It is expected to do so for other Re, as well. It is also beyond the range of reduced velocity at which the hysteretic behavior is observed for Re = 100.

5.3.1. *Mesh convergence study*

To investigate the adequacy of the spatial resolution, for the flow past an oscillating cylinder, two meshes: $M7k$ and $M18k$ are employed for the Re = 100 flow. It was shown earlier, in the paper, that the two meshes result in very similar results for the flow past a stationary cylinder. Mesh $M7k$ is shown in Fig. 1. Mesh $M18k$ is more refined and consists of 18 220 nodes. The domain size for the two meshes is identical. At Re = 100, the cylinder executes high amplitude

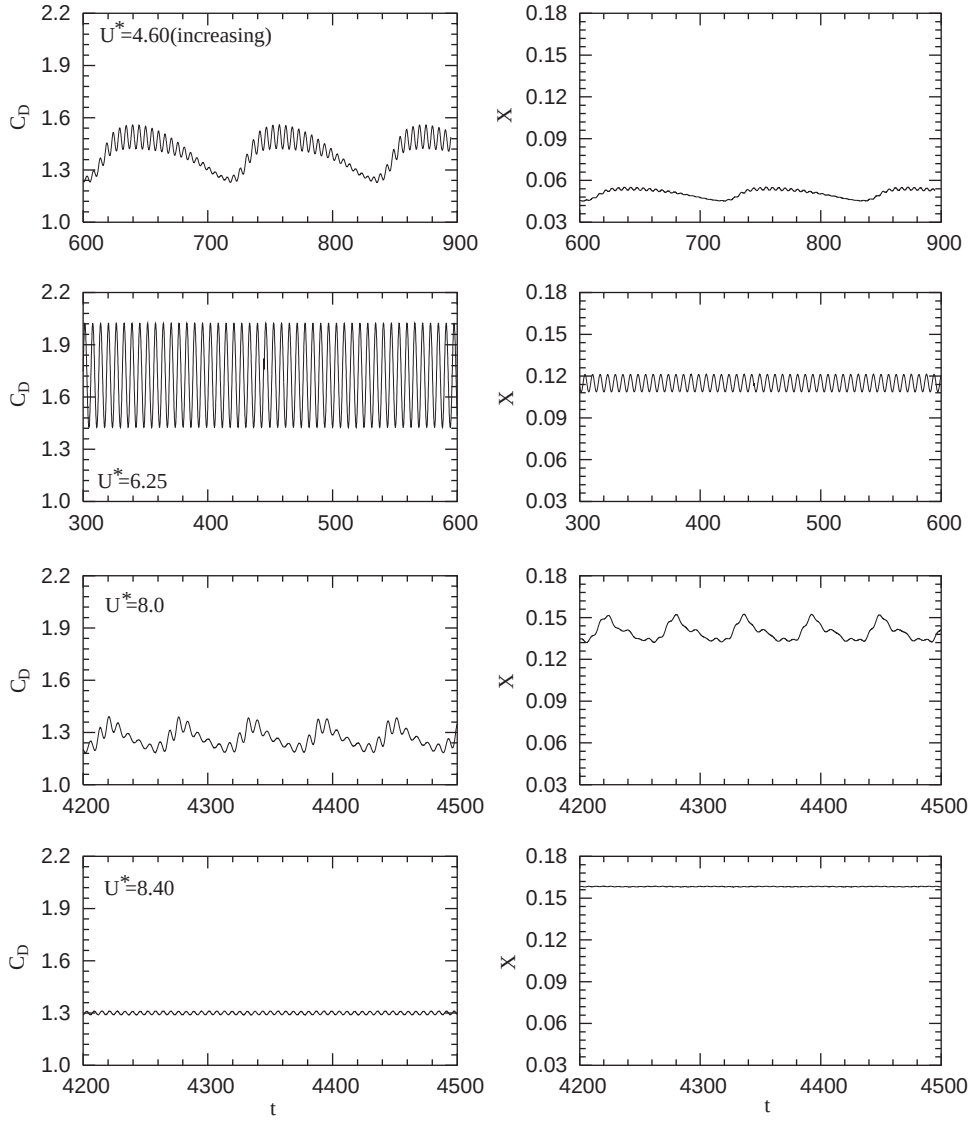

Fig. 9. Vortex-induced vibrations at Re = 100: time histories of the drag coefficient and normalized in-line displacement of the cylinder for various values of reduced velocity, U^*.

vibrations and, therefore, this is a good test case for checking the adequacy of spatial resolution. The summary of the response of the cylinder and the aerodynamic coefficients is shown in Table 1. As was the case with flow past a stationary cylinder, the two meshes result in very similar results. Interestingly, even though the cylinder response predicted from the two meshes are virtually the same, there is a difference of, approximately, 3% between the amplitude of lift coefficients. Overall, the agreement is good and this establishes the adequacy of the mesh *M7k* for the present computations.

5.3.2. *Overview of the cylinder response*

Figs. 10 and 11 show the variation, with Re, of the amplitude of maximum transverse and in-line displacements. Results are presented for Reynolds number between 50 to 500. It is well known that the flow past a cylinder, beyond Re$\sim$200 is associated with three-dimensional effects. In that sense, two-dimensional computations are not expected to give accurate results. However, the objective of the present computations is to study the effect of Re, at a fixed U^*. In particular, we wish to investigate the effect of Re on the modes of vortex shedding for the freely vibrating cylinder.

Table 1
Vortex-induced vibrations for $U^* = 4.92$ and Re = 100: summary of the aerodynamic coefficients and response of the cylinder for two different finite-element meshes.

Mesh	Nodes	Elements	St	$(\frac{Y}{D})_{\max}$	$(\frac{X}{D})_{\text{r.m.s.}}$	$\overline{(\frac{X}{D})}$	$C_{L_{\max}}$	$C_{D_{\max}}$	$C_{D_{\text{r.m.s.}}}$	$\overline{C_D}$
*M*7*k*	7437	7236	0.201	0.57	0.01	0.09	0.96	3.01	0.42	2.39
*M*18*k*	18 220	17 904	0.200	0.57	0.01	0.09	0.93	3.01	0.42	2.38

St is the Strouhal number, $\overline{C_D}$ the mean drag coefficient, $C_{L_{\text{r.m.s.}}}$ the r.m.s. value of the lift coefficient, and $C_{L_{\max}}$ and $C_{D_{\max}}$ are the maximum values of the lift and drag coefficients, respectively. $(\frac{X}{D})_{\text{r.m.s.}}$ and $\overline{(\frac{X}{D})}$ represent the r.m.s. and mean value of the in-line oscillations while $(\frac{Y}{D})_{\max}$ is the maximum value of the amplitude of transverse oscillations.

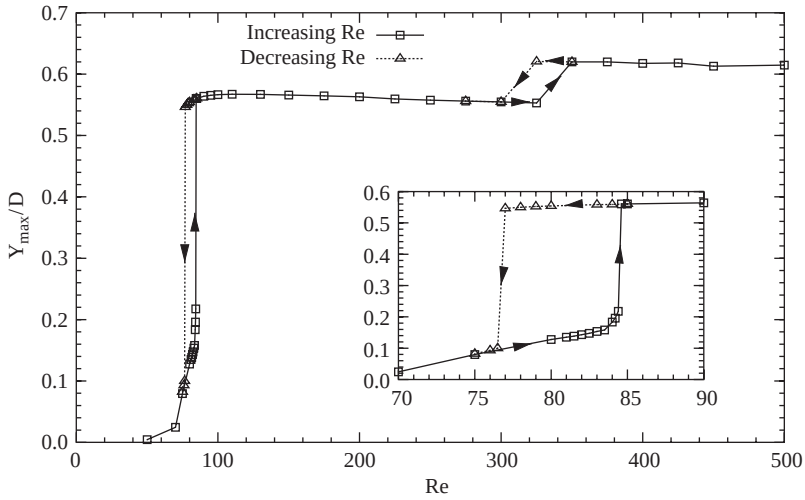

Fig. 10. Vortex-induced vibrations for $U^* = 4.92$: variation of the amplitude of maximum transverse displacement of the cylinder with Re.

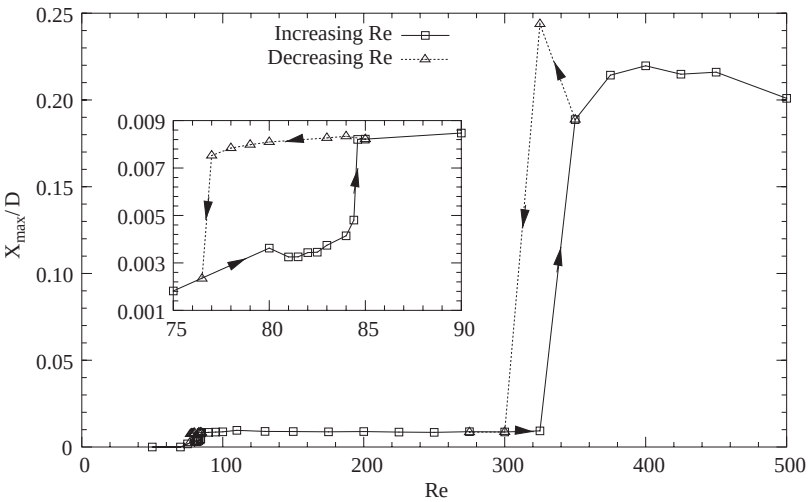

Fig. 11. Vortex-induced vibrations for $U^* = 4.92$: variation of the amplitude of maximum in-line displacement of the cylinder with Re.

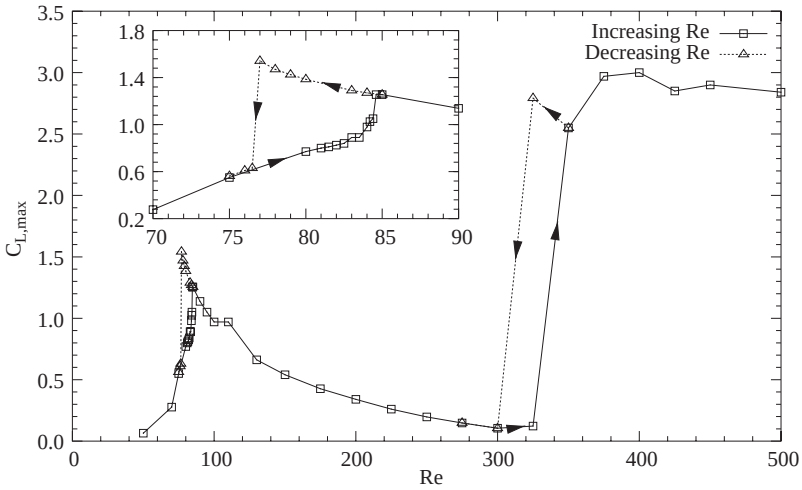

Fig. 12. Vortex-induced vibrations for $U^* = 4.92$: variation of the amplitude of maximum lift coefficient with Re.

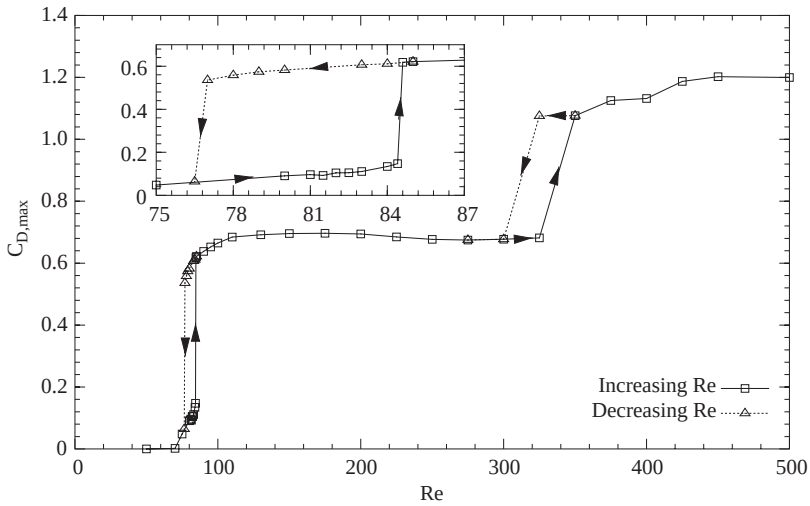

Fig. 13. Vortex-induced vibrations for $U^* = 4.92$: variation of the maximum value of drag coefficient with Re.

At Re$\sim$75 a jump in the amplitude of the transverse oscillations of the cylinder is observed. This jump is hysteretic in nature. The cylinder sustains this level of oscillations till Re$\sim$300, at which point another hysteretic jump to slightly higher amplitude of oscillations is observed. The behavior of the in-line oscillations is quite similar except that the jump in the amplitude at Re$\sim$300 is very large. The variation, with Re, of the amplitude of lift coefficient and the maximum drag coefficient are shown in Figs. 12 and 13. Very large values of the lift coefficient, in excess of 2.5, are observed for Re$>$300.

Fig. 14 shows the variation of the nondimensional shedding frequency, based on the time variation of lift coefficient, with Re. Also shown in the figure is the data for a stationary cylinder from the present computations and from Norberg (2003). The reduced natural frequency of the system ($F_n = 1/U^*$) is also marked on the plot. Very good match between the experimental and present results, for a stationary cylinder, are seen for Re = 100 and less. As expected, at Re = 325 and 350 the present computations lead to slight overprediction of St. For Re$>$200, two-dimensional simulations are known to overpredict the vortex-shedding frequency. For the vibrating cylinder, the vortex-shedding frequency assumes a value quite close to F_n beyond Re$\sim$75. The hysteretic behavior at Re$\sim$75 and 300 are clearly observed from this figure.

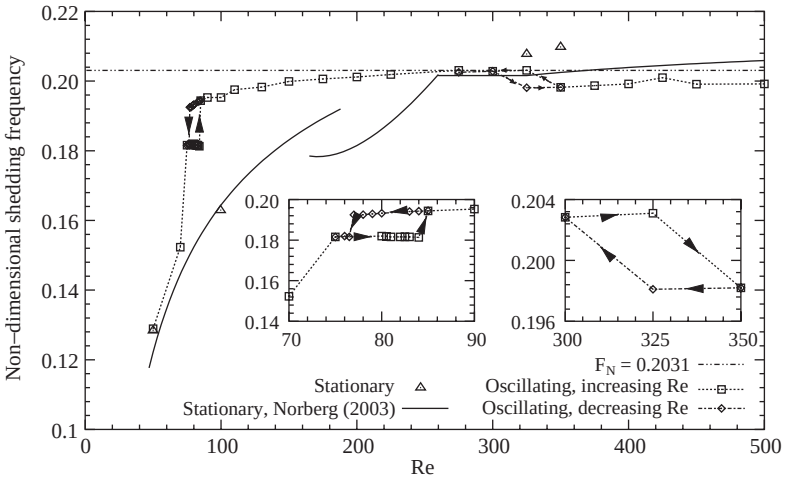

Fig. 14. Vortex-induced vibrations for $U^* = 4.92$: variation of the nondimensional vortex shedding frequency, based on time variation of lift coefficient, with Re. Also shown, is the data for stationary cylinder from the present computations and Norberg (2003).

5.3.3. *A possible cause for the hysteretic jump at* Re∼75

The hysteresis in the first jump at Re∼75 is, perhaps, a consequence of the hysteretic behavior with respect to U^*. Consider a study, similar to as was done for Re = 100 in the previous section, for other values of Re. A behavior similar to the one seen in Fig. 2 is expected. However, the hysteretic transition from the "initial" to "lower" branch is expected to take place at different value(s) of U^*. If all such curves, for various Re are plotted together for a particular value of U^*, a behavior such as shown in Fig. 10 can be expected.

5.3.4. *Vortex-shedding modes*

Fig. 15 shows the vorticity fields for various Re. At Re = 70 the cylinder vibrates with very low amplitude and the flow is very similar to the 2S mode of shedding that is associated with a stationary cylinder at the same Re. At Re = 83, two solutions are realized. The one with lower-amplitude vibrations (increasing Re) exhibits the 2S mode of shedding while the case with higher-amplitude oscillations (decreasing Re) is associated with the C(2S) mode [as described by Williamson & Roshko (1988)]. The C(2S) mode is very similar to the 2S mode except that vortices coalesce in far wake. The cylinder continues to shed vortices in the C(2S) mode till Re∼300.

Re = 325 is associated with two distinct modes of vortex shedding. The 2S mode is observed for the increasing Re branch. The solution corresponding to decreasing Re shows the P + S mode of vortex shedding. In this mode, in each cycle of shedding, a single vortex and a pair of counter-rotating vortices are released from the cylinder. This mode of shedding is also observed for higher Re (see Fig. 15 for Re = 350 and 425). Meneghini and Bearman (1995) carried out numerical simulations for the Re = 200 flow with forced vibrations of the cylinder. They found that the P + S mode of shedding exists for Re = 200 flow when the amplitude of vibrations of the cylinder is larger than ∼0.6D. The 2S mode is observed when the amplitude of vibrations is less than ∼0.6D. Interestingly, the present results show that the amplitude of transverse vibrations with the 2S mode of shedding is ∼0.56D while it is ∼0.62D with the P + S mode of shedding. Blackburn and Henderson (1996) also found from their simulations, for Re = 140 flow with forced vibrations of the cylinder, that the P + S mode of vortex shedding is observed for oscillation amplitude of 0.75D and higher. Williamson and Govardhan have pointed out that although this mode of shedding is excited by forced vibrations, it has never been observed earlier in free vibrations. This point certainly needs more investigation and further work is being done to understand the mechanism of energy transfer between the fluid and the vibrating cylinder. Our observations are in line with the work by Blackburn and Henderson (1999). They simulated two-dimensional flow past a cylinder with forced cross-flow oscillations at Re = 500. Various frequency ratios were simulated with oscillation amplitude of 0.25D. They studied the mechanical energy transferred from the fluid to the oscillating cylinder during one cycle of its motion. Four branches of the variation of the energy with frequency were identified. On one of the branches, corresponding to the P + S mode of shedding, a positive transfer of energy from the flow to the cylinder was observed. This shows that free vibrations with the P + S mode, in a two-dimensional setup, are possible.

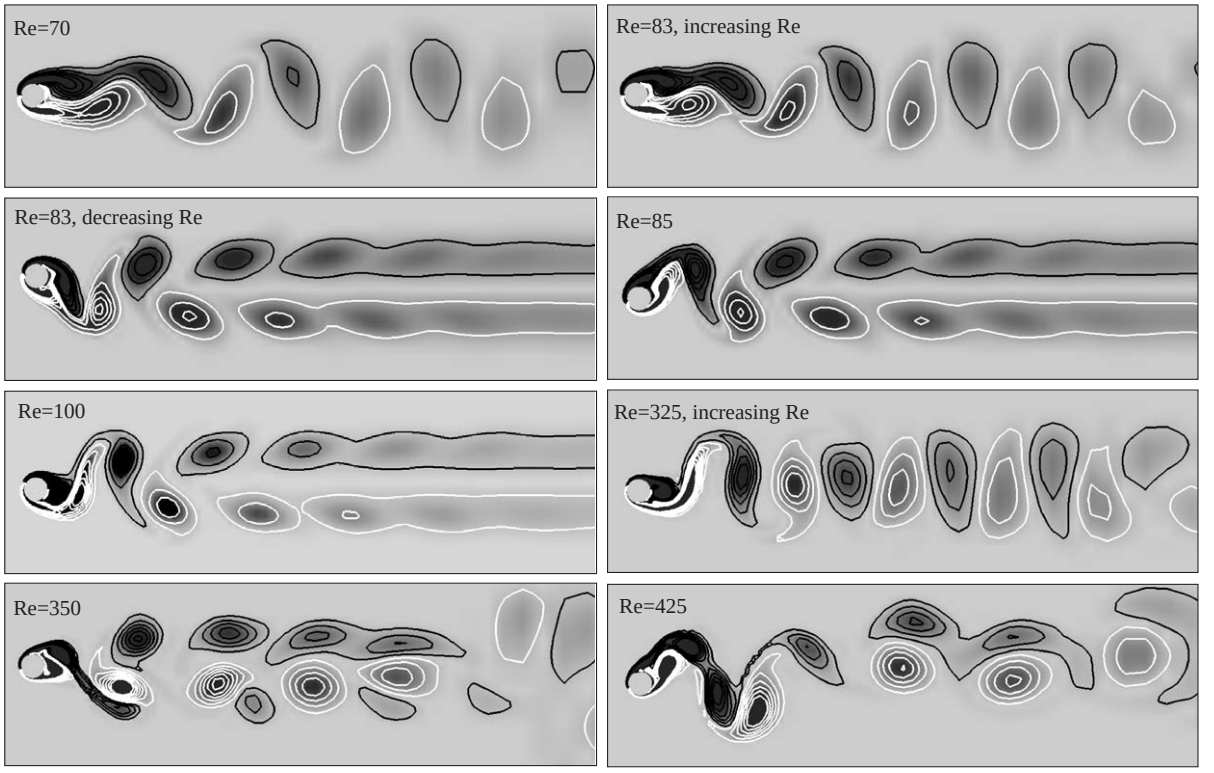

Fig. 15. Vortex-induced vibrations for $U^* = 4.92$: instantaneous vorticity field for various Re.

5.3.5. Competition/switching in modes of vortex shedding

As seen from the response of the cylinder in Figs. 10 and 11, there is a hysteretic jump in the oscillation amplitude at Re$\sim$300. This is accompanied with a change in the mode of vortex shedding. Fig. 16 shows the time history of the lift coefficient and instantaneous vorticity field at various times. Both, 2S and P + S modes of vortex shedding are observed at different instants of time. For example the flow at $t = 625$ corresponds to the 2S mode. At $t = 1875$, the mode of shedding is P + S while it is C(2S) at $t = 4125$. This points to competition/switching between the various modes of shedding.

Fig. 17 shows the time history of the lift coefficient and instantaneous vorticity field at various times for the Re = 325 flow for the solution corresponding to the decreasing Re branch. As is the case with the Re = 375 flow, competition/switching between the P + S and 2S modes of vortex shedding can be observed here, as well. In addition, the flip-flop between the two mirror images of the P + S mode of shedding is also seen. It is found, from the frequency spectra, that the dominant frequencies in the time variation of the lift coefficient and cylinder response in the transverse direction are very close. This implies synchronization/lock-in between the cylinder motion and the flow. This is also observed from Fig. 18 which shows the close-up view of the two time histories. Also shown in the same figure, for comparison, are the time histories for the Re = 325 flow corresponding to the 2S mode of shedding for increasing Re. The time histories for the latter appear to be more organized and periodic. It is, perhaps, for the first time that the P + S mode of vortex shedding has been observed in free-vibrations. Computations with a more refined finite-element mesh produced same results. Interestingly, it was also found that the free vibration computations for Re = 325 initiated with the flow past a stationary cylinder at the same Re lead to the solution corresponding to the high amplitude of oscillations.

To investigate the role of in-line oscillations in the mode competition at Re = 325, a computation in which the cylinder is restricted to cross-flow oscillations (no in-line oscillations) was carried out for the decreasing Re branch. In this case the 2S mode of vortex shedding is not observed; only the P + S mode of vortex shedding is seen. The amplitude of cross-flow oscillations in the two cases, with and without in-line oscillations, is quite comparable.

The power spectra of the time histories of the drag coefficient for the Re = 325 flow for the increasing Re (2S mode of shedding) and decreasing Re (P + S mode of shedding) were compared. For the case corresponding to the 2S mode of shedding only one peak is observed; the drag oscillates at, approximately, twice the natural frequency of the oscillator.

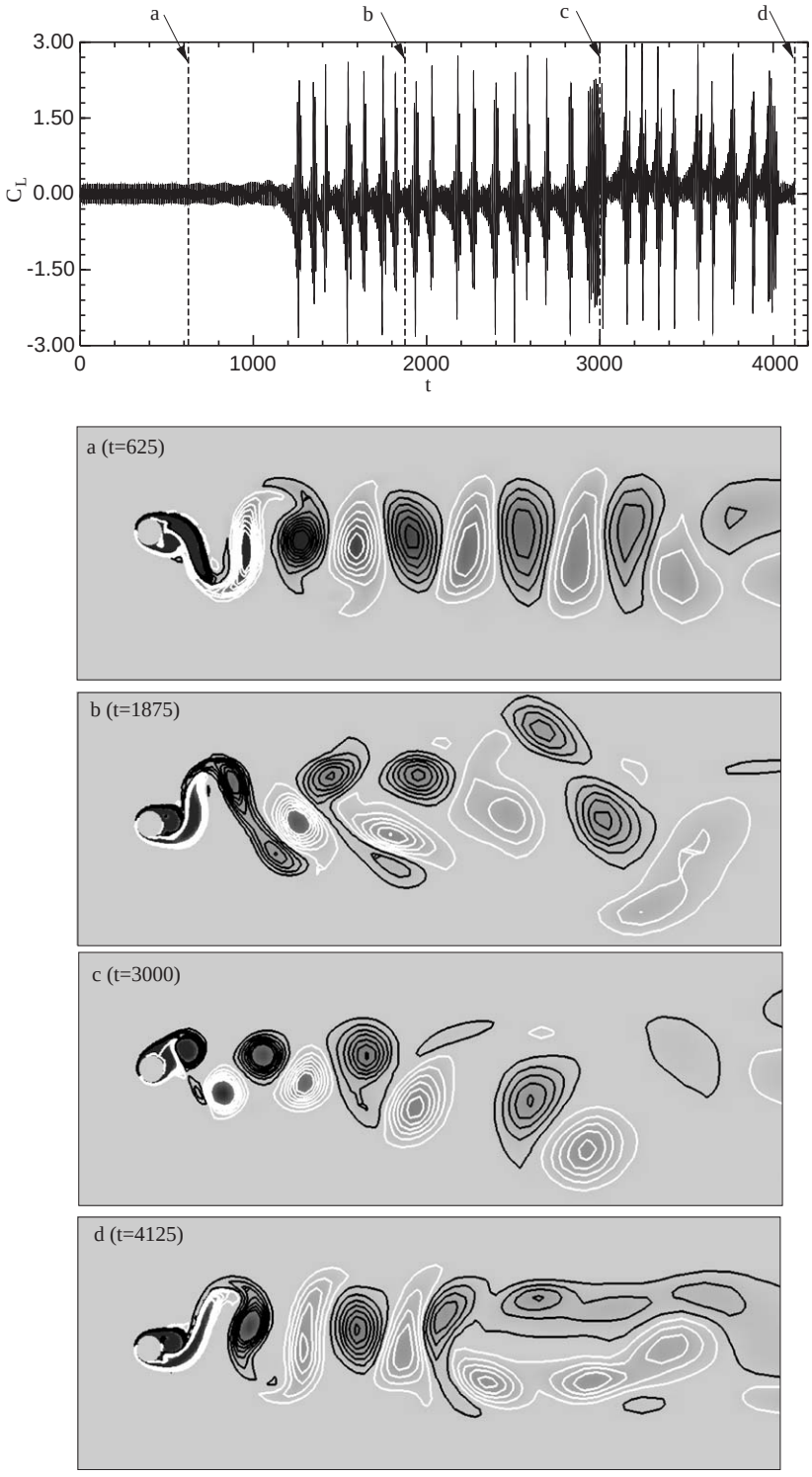

Fig. 16. Vortex-induced vibrations for $U^* = 4.92$ and $\mathrm{Re} = 375$: time history of the lift coefficient and the instantaneous vorticity field various time instants.

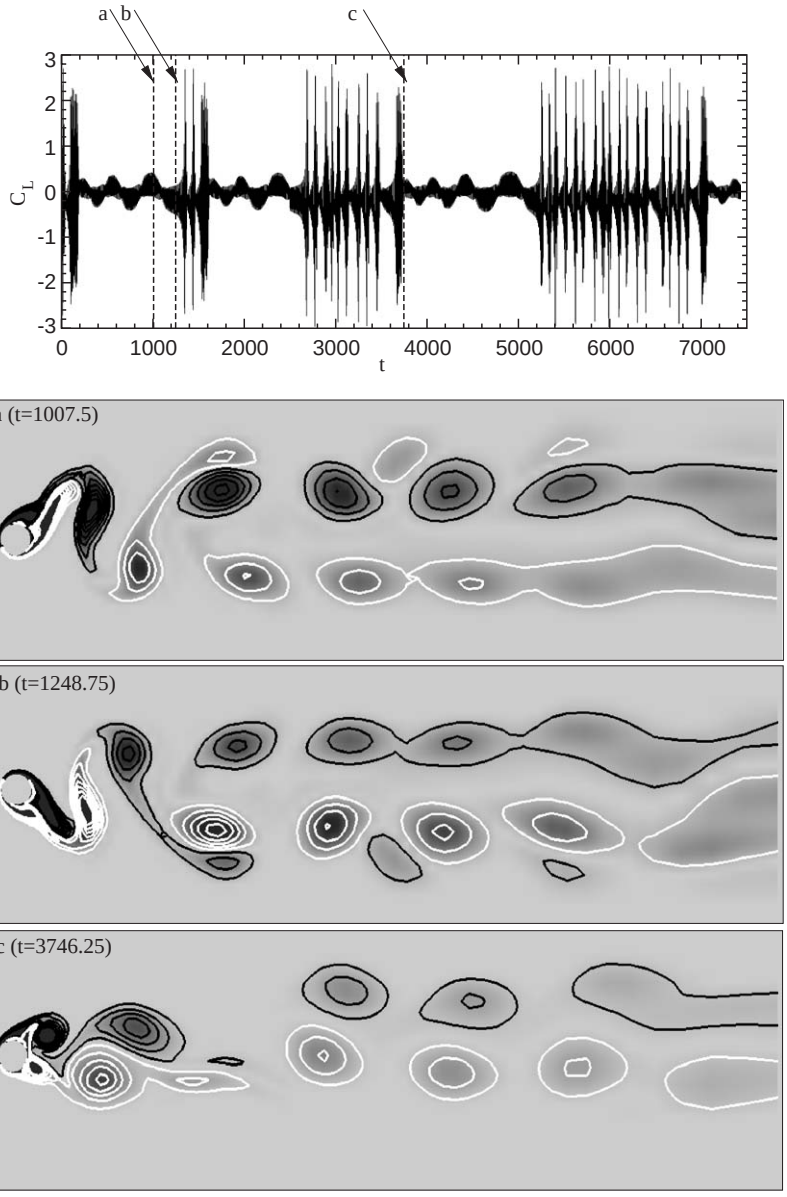

Fig. 17. Vortex-induced vibrations for $U^* = 4.92$ and $\mathrm{Re} = 325$ (decreasing Re): time history of the lift coefficient and the instantaneous vorticity field various time instants.

However, for the P + S mode of shedding there is an additional peak that corresponds to the natural frequency of the oscillator. This might explain the significant increase in the in-line oscillation amplitude of the cylinder motion with the P + S mode of shedding for these two-dimensional simulations.

6. Conclusions

Vortex induced vibrations of a cylinder, at low Re, are simulated numerically via a stabilized finite element method applied to the incompressible flow equations in primitive variables. The effect of reduced velocity and Re have been studied. To this extent, two sets of simulations have been carried out: (i) Re set to 100 and U^* is varied, (ii) computations at various Re for $U^* = 4.92$.

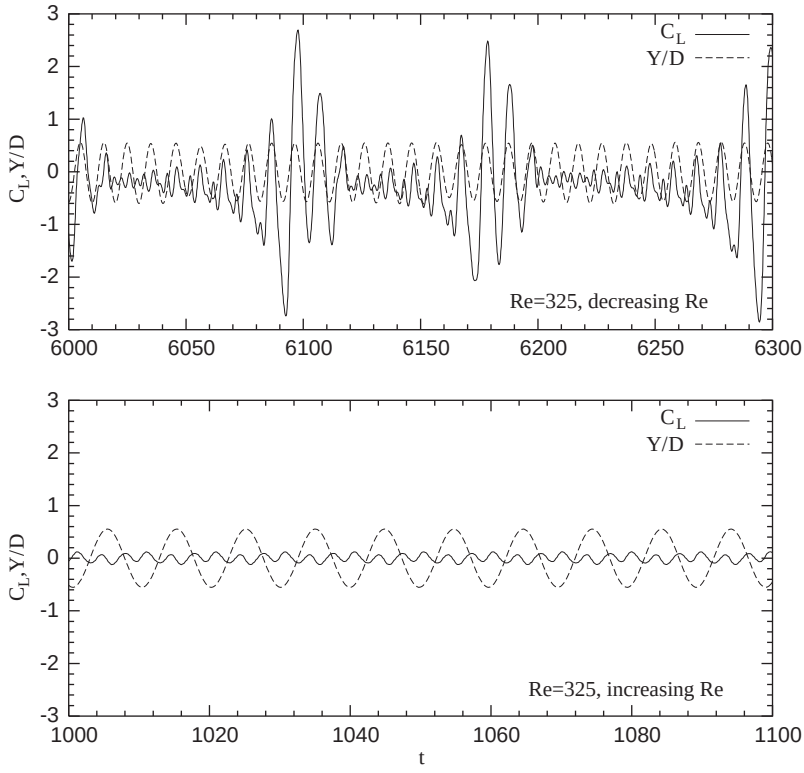

Fig. 18. Vortex-induced vibrations for $U^* = 4.92$ and $\mathrm{Re} = 325$: close-up view of the time histories of the lift coefficient and the transverse displacement of the cylinder.

For the first time, hysteretic jump from the initial- to low-amplitude branch, at lower end of the synchronization range of reduced velocity, in the laminar vortex-shedding regime have been observed. A careful examination of the details in the region of jump ($4.4 \leqslant U^* \leqslant 4.7$) shows that there are two distinct loops of hysteresis. While the mode of vortex shedding with low amplitude of vibrations of the cylinder is 2S, it is C(2S) when the oscillation amplitude is large. It is found that the jump at the higher end of the synchronization range of reduced velocity is also hysteretic. Computations with *transverse only* and *in-line only* oscillations confirm that this hysteresis is not a consequence of the in-line oscillations. The maximum amplitude for transverse and in-line oscillations is achieved for $U^* \sim 4.75$ and 8.25, respectively. In the laminar vortex-shedding regime, the in-line oscillation amplitude is quite small compared to the amplitude of transverse oscillations.

It is found that the effect of Re, for a vibrating cylinder, is quite significant. For $\mathrm{Re} < 300$, the vortex shedding takes place in the 2S mode. At larger Re, the P + S mode also appears. This mode of shedding has been observed for the first time for a freely vibrating cylinder. The change in mode of shedding is accompanied with a very large increase in the amplitude of in-line oscillations. A slight increase in the amplitude of transverse oscillations is observed, as well. It is known that the flow ceases to remain two-dimensional beyond $\mathrm{Re} \sim 200$. Therefore, it remains to be seen whether the P + S mode of shedding can actually be observed in reality.

Acknowledgements

Partial support for this work has come from the Department of Science and Technology, India.

References

Anagnostopoulos, P., Bearman, P.W., 1992. Response characteristics of a vortex excited cylinder at low reynolds number. Journal of Fluids and Structures 6, 39–50.

Blackburn, H., Henderson, R., 1996. Lock-in behavior in simulated vortex-induced vibration. Experimental Thermal and Fluid Science 12, 184–189.

Blackburn, H., Henderson, R., 1999. A study of two-dimensional flow past an oscillating cylinder. Journal of Fluid Mechanics 385, 255–286.

Brika, D., Laneville, A., 1993. Vortex-induced vibrations of a long flexible circular cylinder. Journal of Fluid Mechanics 250, 481–508.

Guilmineau, E., Queutey, P., 2001. Numerical simulation in vortex-induced vibrations at low mass-damping. In: AIAA 24th Fluid Dynamics Conference & Exhibit, AIAA-2001-3099.

Henderson, R.D., 1995. Details of the drag curve near the onset of vortex shedding. Physics of Fluids 7, 2102–2104.

Jauvtis, N., Williamson, C.H.K., 2003. Vortex-induced vibration of a cylinder with two degrees of freedom. Journal of Fluids and Structures 17, 1035–1042.

Khalak, A., Williamson, C.H.K., 1999. Motions, forces and mode transitions in vortex-induced vibrations at low mass-damping. Journal of Fluids and Structures 13, 813–851.

Koopmann, G.H., 1967. The vortex wakes of vibrating cylinders at low Reynolds numbers. Journal of Fluid Mechanics 28, 501–512.

Kravchenko, A.G., Moin, P., Shariff, K., 1999. B-Spline method and zonal grids for simulations of complex turbulent flows. Journal of Computational Physics 151, 757–789.

Mittal, S., 1992. Stabilized space–time finite element formulations for unsteady incompressible flows involving fluid-body interactions. Ph.D. Thesis, University of Minnesota.

Mittal, S., Kumar, V., 1999. Finite element study of vortex-induced cross-flow and in-line oscillations of a circular cylinder at low Reynolds numbers. International Journal for Numerical Methods in Fluids 31, 1087–1120.

Mittal, S., Tezduyar, T.E., 1992. A finite element study of incompressible flows past oscillating cylinders and airfoils. International Journal for Numerical Methods in Fluids 15, 1073–1118.

Meneghini, J.R., Bearman, P.W., 1995. Numerical simulation of high amplitude oscillatory flow about a circular cylinder. Journal of Fluids and Structures 9, 435–455.

Norberg, C., 2003. Fluctuating lift on a circular cylinder: review and new measurement. Journal of Fluids and Structures 17, 57–96.

Persillon, H., Braza, M., 1998. Physical analysis of the transition to turbulence in the wake of a circular cylinder by three-dimensional Navier–Stokes simulation. Journal of Fluid Mechanics 365, 23–88.

Tezduyar, T.E., Behr, M., Liou, J., 1992a. A new strategy for finite element computations involving moving boundaries and interfaces—the deforming-spatial-domain/space–time procedure, I: the concept and the preliminary tests. Computer Methods in Applied Mechanics and Engineering 94 (3), 339–351.

Tezduyar, T.E., Behr, M., Mittal, S., Liou, J., 1992b. A new strategy for finite element computations involving moving boundaries and interfaces—the deforming-spatial-domain/space–time procedure, II: computation of free-surface flows, two-liquid flows, and flows with drifting cylinders. Computer Methods in Applied Mechanics and Engineering 94 (3), 353–371.

Tezduyar, T.E., Mittal, S., Ray, S.E., Shih, R., 1992c. Incompressible flow computations with stabilized bilinear and linear equal-order-interpolation velocity–pressure elements. Computer Methods in Applied Mechanics and Engineering 95, 221–242.

Williamson, C.H.K., 1989. Oblique and parallel modes of vortex shedding in the wake of a circular cylinder at low Reynolds numbers. Journal of Fluid Mechanics 206, 579–627.

Williamson, C.H.K., 1996. Vortex dynamics in the cylinder wake. Annual Review of Fluid Mechanics 28, 477–539.

Williamson, C.H.K., Govardhan, R., 2004. Voretx-induced vibration. Annual Review of Fluid Mechanics 36, 413–455.

Williamson, C.H.K., Roshko, A., 1988. Vortex formation in the wake of an oscillating cylinder. Journal of Fluids and Structures 2, 355–381.

Further reading

Williamson, C.H.K., 1988. The existence of two stages in the transition to three-dimensionality of a cylinder wake. Physics of Fluids 31 (11), 3165–3168.